Flexible CO₂ Sensor Architecture with Selective Nitrogen Functionalities by One-Step Laser-Induced Conversion of Versatile Organic Ink

Huize Wang, Charles Otieno Ogolla, Gyanendra Panchal, Marco Hepp, Simon Delacroix, Daniel Cruz, Danny Kojda, Jim Ciston, Colin Ophus, Axel Knop-Gericke, Klaus Habicht, Benjamin Butz,* and Volker Strauss*

Nitrogen-containing carbons (NC) are a class of sustainable materials for selective CO_2 adsorption. A versatile concept is introduced to fabricate flexible NC-based sensor architectures for room-temperature sensing of CO_2 in a one-step laser conversion of primary films cast from abundant precursors. By the unidirectional energy impact in conjunction with depth-dependent attenuation of the laser beam, a layered sensor heterostructure with a porous transducer and active sensor layer is formed. Comprehensive microscopic and spectroscopic cross-sectional analyses confirm the preservation of the high content of imidazolic nitrogen in the sensor. The performance is optimized in terms of material morphology, chemical composition, and surface chemistry to achieve a linear relative resistive response of up to $\Delta R/R_0 = -14.3\%$ (10% of CO_2). Thermodynamic analysis yields $\Delta_{ads}H$ values of -35.6 and 34.1 kJ·mol^{-1} for H_2O and CO_2, respectively. The sensor is operable even in humid environments (e.g., $\Delta R/R_{0,RH=80\%} = 0.53\%$) and shows good performance upon strong mechanical deformation.

1. Introduction

Monitoring CO₂ is imperative to understand its origin and impact. Both, the global climate crisis and the current COVID-19 pandemic have shifted attention and created awareness of the need for comprehensive CO₂ monitoring on local and global scales.[1,2] To fight global warming, a deeper awareness of the public of the impact of greenhouse gases like CO₂ may be required. In industrial and work environments, high concentrations of CO₂ (in)directly pose health risks due to acidosis or the enrichment of undesired species like viruses, or may cause performance loss even during office work.[3] Capable smart mobile devices and flexible wearables to collect exhaled breath may support decentralized healthcare as well as professional and amateur sport.[4]

Handheld or stationary infrared absorption sensors represent state-of-the-art device technology but exhibit limitations regarding versatility, compactness, and integrability.[5] Integrated micro-sensors, with a superior property portfolio including small size, flexibility, and low cost would facilitate comprehensive spatial and temporal analyses of CO₂ in a wide range of applications.[6]

Thus, the development of simple miniaturized sensors with a rapid response for a wide range of CO₂ concentrations has

H. Wang, V. Strauss
Max-Planck-Institut für Kolloid- und Grenzflächenforschung
Am Mühlenberg 1, 14476 Potsdam, Germany
E-mail: volker.strauss@mpikg.mpg.de
C. O. Ogolla, M. Hepp, B. Butz
Micro-and Nanoanalytics Group
University of Siegen
Paul-Bonatz Str. 9–11, 57076 Siegen, Germany
E-mail: benjamin.butz@uni-siegen.de
G. Panchal, D. Kojda, K. Habicht
Dept. Dynamics and Transport in Quantum Materials
Helmholtz-Zentrum Berlin für Materialien und Energie GmbH
Hahn-Meitner-Platz 1, 14109 Berlin, Germany

S. Delacroix
LPICM
CNRS UMR 7647
Ecole polytechnique
Institut Polytechnique de Paris
91128 Palaiseau, France
D. Cruz, A. Knop-Gericke
Department of Inorganic Chemistry
Fritz-Haber-Institut der Max-Planck-Gesellschaft
Faradayweg 4–6, 14195 Berlin, Germany
D. Cruz, A. Knop-Gericke
Department of Heterogeneous Reactions
Max Planck Institute for Chemical Energy Conversion
Stiftstraße 34–36, 45470 Mülheim an der Ruhr, Germany
J. Ciston, C. Ophus
National Center for Electron Microscopy
Molecular Foundry
Lawrence Berkeley National Laboratory
1 Cyclotron Road, Berkeley, California, USA
K. Habicht
Institut für Physik und Astronomie
Universität Potsdam
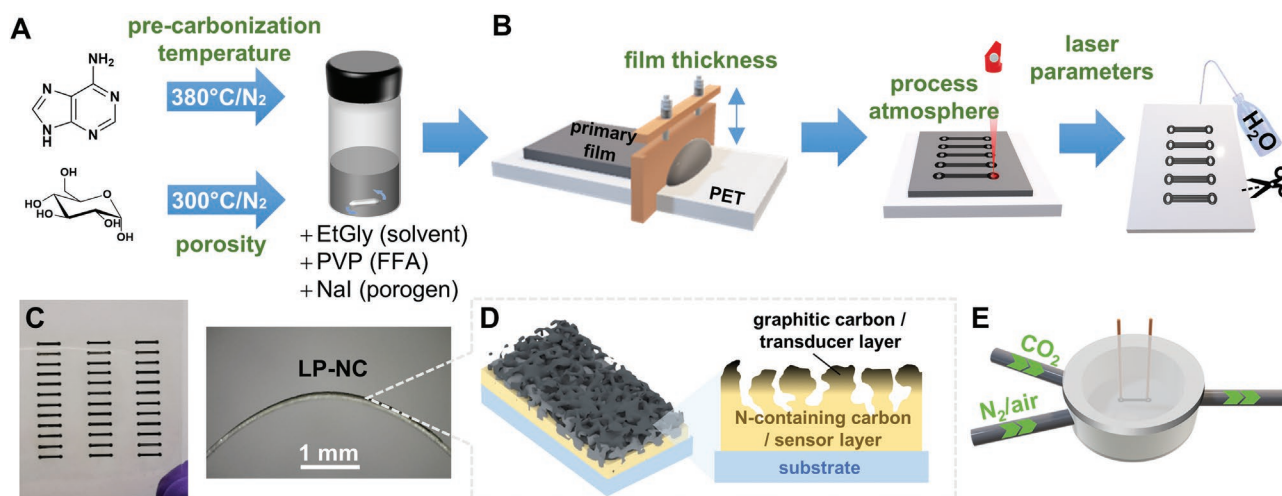Karl-Liebknecht-Str. 24-25, 14476 Potsdam, Germany

**ADVANCED
SCIENCE NEWS**

www.advancedsciencenews.com

**ADVANCED
FUNCTIONAL
MATERIALS**

www.afm-journal.de

Figure 1. Scheme of sensor fabrication, optimization, and testing: A) Pyrolysis of adenine/glucose, mixing with porogen, film-forming agent, and solvent to obtain a viscous ink; B) Coating by doctor-blading and subsequent laser-patterning in different atmospheres; C) Photographs of a 20 cm² PET substrate with 36 LP-NC sensor strips (left) and a single sensor strip on flexible PET bent in positive direction (right); D) Schematic of the "inverted" sensor architecture of an LP-NC sensor with the graphitized carbon transducer layer and the N-containing carbon sensor layer; E) Illustration of the gas-sensing cell used to characterize the resistive response of the LP-NC sensors in different environments.

attracted the attention of materials scientists.[7] Device concepts are typically based on synthetically functionalized or hybridized (with metals or metal oxides) carbon nanomaterials (CNM) to provide specific active sites on their surface or to tune their electronic properties, respectively.[8,9] However, relatively high costs, associated with the sophisticated materials and fabrication processes, are still a challenge for commercialization.[10]

A promising inexpensive alternative is tailored nitrogen-containing carbons (NCs). Such NCs, obtained from pyrolysis, are a class of materials, which has been proposed for selective CO_2 capture or conversion as they intrinsically provide selective binding sites for CO_2.[11–15] In particular, polypyrrole or imidazole-based NCs demonstrate a remarkable CO_2 sorption capacity as well as excellent environmental stability and electrical conductivity.[16–18] Like CNMs, those particulate NCs require additional processing steps to generate complex sensor architectures.

Considering that simple, fast, and cost-effective processing makes a difference in applicability, printing technologies are a favored solution as they minimize fabrication costs and personal training procedures.[19] In the past decade, laser processing has become popular for the fabrication of flexible miniaturized chemical[20–23] and mechanical[24–26] sensors[27] but also other flexible d. Commonly, porous laser-patterned carbon (LP-C) films with tailored properties are obtained by laser treatment of, for example, graphene oxide,[28] polyimides,[29] or lignins.[30] Typical strategies for sensor improvements for gaseous or liquid analytes include detection by a change of the thermal conductivity, by incorporation of heterojunctions, or post-functionalization.[20–27] In contrast to using polymeric precursors, naturally abundant, molecular compounds as starting materials provide enhanced versatility to engineer materials by implementing specific functional groups during their fabrication.[31]

This study demonstrates that the proposed concept of single-step laser-patterning of optimized organic precursor coatings enables the fabrication of tailored sensor heterostructures even on flexible substrates. Here, we present a complete architecture for CO_2 sensing on polyethyleneterephthalate (PET).[32] The flexible nitrogen-containing LP-C (LP-NC) sensors exhibit high sensitivity to CO_2 and a decent degree of selectivity even in humid environments in conjunction with good cycling stability and excellent mechanical properties. Adenine was used as the major precursor due to its rich nitrogen functionalities; glucose and sodium iodide were employed as foaming agents and porogen, respectively. The fabrication process was optimized in terms of precursor synthesis, primary film composition/thickness, laser parameters, and reaction atmosphere to enhance the sensor response. The performance for CO_2 sensing was proven in dry as well as humid environments. Structure formation and operating principle of the complex sensor were elucidated by comprehensive micro- and nanoanalyses.

2. Results and Discussion

2.1. Design of CO_2 Gas Sensor and Processing

Laser-patterned LP-NC sensors (0.5×5 mm with enlarged end electrodes) were realized in a resistive sensor design. The integrated approach includes ink optimization/preparation, film-casting, and laser-carbonization (**Figure 1**A,B). The precursor ink combines functionalities of pre-carbonized adenine ($C_5N_5H_5$) as nitrogen-rich precursor, pre-carbonized glucose as foaming agent[33] (and additional carbon source), sodium iodide (NaI) as porogen,[34] and polyvinylpyrrolidone (PVP) as film-forming agent (FFA).[35] Those were dissolved in ethylene glycol (EtGly) and the resulting ink was cast onto flexible polyethyleneterephthalate (PET) substrates of 20 cm[2] by doctor-blade coating.

The primary films were irradiated with a mid-infrared CO_2-laser under different atmospheres (air, N_2, or O_2) to create

**ADVANCED
SCIENCE NEWS**
www.advancedsciencenews.com

**ADVANCED
FUNCTIONAL
MATERIALS**
www.afm-journal.de

the LP-NC sensor strips. The unexposed precursor material was rinsed off the substrates with deionized water. By laser treatment, we produce an "inverted" sensor architecture with a graphitized carbon transducer layer (upper layer) and N-containing carbon sensor layer (lower layer) inside each sensor film (Figure 1D). A typical electrical or electrochemical sensor architecture is composed of 1) a high-surface area sensor material with specific binding sites and 2) a conductive transducer material that transmits the signal to a 3) read-out unit. In the present case, the conductive transducer material evolves as a porous graphitic carbon network on top of the sensor layer.

In each batch, 36 gas sensor strips were produced in only 144 s (Figure 1C). Subsequently, the LP-NC strips were tested as resistive sensor platforms to detect CO_2 at room temperature in a gas-flow cell (Figure 1E). To enhance the sensor response toward CO_2, the pre-carbonization parameters, laser parameters, process atmosphere, ink composition, and coating thickness were optimized.

2.2. Materials and Process Optimization

2.2.1. Screening CNFA Reaction Temperature

Pre-carbonization of molecular precursors is a requirement for laser-carbonization, as it condenses the precursors and supports the formation of a conductive LP-C film (**Figure 2**A).[31] In a temperature range of 300–400 °C, adenine undergoes condensation, which is revealed by a color change and a reduction of the N-content (formation of carbon-network forming agent: CNFA) (p. S2, Figure S1, Supporting Information).

To be applicable as chemiresistive sensors, the electric conductivity (σ) of LP-NC and the change of resistance upon exposure to 10% CO_2 (response: $\Delta R/R_0$) are essential factors. We tested the influence of the pre-carbonization temperature on σ of the LP-NC (produced under air) and their response to exposure to 10% CO_2. The LP-NC films produced from the different CNFAs are named LP$_{air}$_Ade300 – LP$_{air}$_Ade400. In Figure 2A, the conductivity and response to exposure of 10%

CO_2 of these films are plotted. LP$_{air}$_Ade300 and LP$_{air}$_Ade320, and LP$_{air}$_Ade400 are not conductive while the highest conductivity of 30.6 S cm^{-1} is observed for LP$_{air}$_Ade340. In initial sensing experiments, we found that LP$_{air}$-Ade380 shows the highest $\Delta R/R_0$ values in comparison to the precursors annealed at lower or higher temperatures (Figure 2A). For all subsequent experiments, we used the Ade380 as the standard CNFA. Glucose was pre-carbonized at 300°C according to the previous optimization.[31]

2.2.2. Laser Parameters

As recently demonstrated, each CNFA shows a characteristic response to the laser processing parameters, i.e., the incident power and scanning speed.[31] Optimal scan speeds of 189 cm s^{-1} and laser power of 1.1 W (pp. S2–S3, Figure S2, Supporting Information) were obtained by optimizing the conductivity and performance of reference LP-NCs (pure adenine-CNFA).

2.2.3. Process Atmosphere

Moreover, the reaction atmosphere is a critical factor for the resulting properties (Figure 2B), as laser-patterning involves pyrolysis and combustion processes, and the surface polarity induced by oxygenation was found to improve the sorption of CO_2. When changing from N_2 or air to a pure O_2 atmosphere, the resistive response was increased by more than one order of magnitude from $\Delta R/R_0$ = −0.22% to -3.2% for LP$_{O2}$-Ade380 at 10% CO_2 exposure, while the LP-NC morphology is only marginally influenced by the reaction atmosphere (p. S3, Figure S3, Supporting Information).

2.2.4. Porosity – Foaming Agent

Increasing porosity leads to improving the accessibility of CO_2 to active sites in the film. Glucose is a well-known precursor for
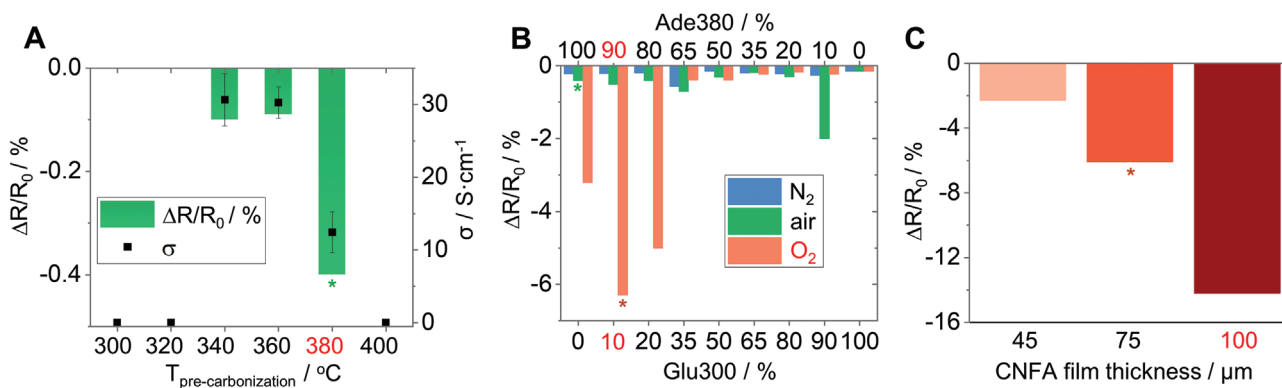

Figure 2. Materials and process optimization: A) Dependency of electric sheet conductivity (black dots) and resistive response (green) on pre-carbonization temperature of adenine (LP$_{air}$-Ade300–400) upon exposure to 10% CO_2:90% N_2 (starting coating thickness 75 μm, optimized pre-carbonization temperature highlighted in red; green star symbol referring to the same sample in B); B) Resistive response (10% CO_2:90% N_2) of pure and mixed LP-NC heterostructures upon laser-treatment in different environments (N_2, O_2, air) (optimized composition highlighted in red; orange star symbol referring to the same sample in C); C) Resistive response of LP$_{O2}$-Ade380$_{90}$/Glu300$_{10}$ sensors, laser-treated in oxygen, with different thickness of 45, 75, and 100 μm upon exposure to 10% CO_2:90% N_2.

carbonized materials that generate high surfaces by foaming. In this study, we use pre-carbonized glucose (Glu300) as a CNFA in laser patterning, and a carbon foam is obtained. Bubbles in a size range between tens of nanometers up to several microns are observed (Figure S4, Supporting Information). This foaming effect of Glu300 during laser-carbonization is used to increase the porosity of the LP-NC. To test this hypothesis nine compositions with different mixing ratios of Ade380 (N-source) and Glu300 (foaming agent) were tested for the response toward 10% CO_2 (Figure 2B; p. S4, Figure S4, Supporting Information). As both, high concentrations of active N-sites and good access to those sites by sufficient porosity are required, LP-NC films with a significant fraction of glucose-CNFA yield the highest responses., i.e., the best response is obtained for adding 10 wt% of Glu300 to the Ade380 precursor film (LP_{O2}-$Ade380_{90}$/$Glu300_{10}$) produced under O_2 reaching $\Delta R/R_0 = -6.3\%$. Therefore, for the optimized sensor, comprehensively investigated in this study, a CNFA ratio of 90:10 wt% (adenine-CNFA:glucose-CNFA) was used.

2.2.5. Film thickness

The response of LP_{O2}-$Ade380_{90}$/$Glu300_{10}$ was finally enhanced to $\Delta R/R_0 = -14.3\%$ by increasing the thickness of the initial precursor coating from 75 to 100 μm (Figure 2C), while the response of the 45 μm film was much reduced (Figure 2C). This is owing to a reduced number of active sites in the lower layers. In fact, a balance between the severely graphitized upper layer and the preservation of active N-sites in the lower layers is required to form an efficient two-layer sensor heterostructure. However, further increase of the thickness leads to delamination (e.g., materials loss upon rinsing).

2.3. Microstructure and chemistry of sensor architecture

To unravel the structure formation and functionality of the LP_{O2}-$Ade380_{90}$/$Glu300_{10}$ sensor with its N and O functionalities, a comprehensive investigation of the film morphology, local composition/bonding, and structure was carried out (**Figure 3**). Throughout the entire laser-irradiated area the films show a typical open-porous morphology[35] (Figure 3A,C,D; Figure S5, Supporting Information) facilitated by the synergistic foaming effects of Glu300 and NaI. The depth-dependent attenuation of the irradiation was successfully utilized in one-step laser treatment to create the lateral heterostructure with transducer and sensor sub-layers (Figure 3C,D). Strongly different morphologies of the two layers in terms of composition and structure (Figure 3C–F; Figure S5, Supporting Information) afford their different functions. The excellent mechanical integrity and good interconnection are reflected in the cross-sectional data as well as in the sensing tests upon repeated elastic bending (Figure 4F).

The granular starting morphology with μm-sized glucose/adenine-CNFA particles is proven by cross-sectional SEM-EDXS (Figure 3C). To distinguish between device regions from the glucose-CNFA and the embedding resin, the local presence of the porogen NaI is considered. The homogeneous

Na distribution within the sensor layer in contrast to the patchy N-distribution confirms a few μm-sized regions, which are attributed to the globular glucose-based CNFA within the N-containing matrix.

Extensive pore formation occurs during laser treatment. In the upper transducer layer, open, interconnected macropores are generated as indicated by the complete infiltration by epoxy resin (Figure 3C,D). That pore network ensures excellent accessibility to the active N-sites of the sensor layer by the analyte and carrier gas. Only a sparse network of graphitized carbon remains, which is laterally interconnected and ensures a sufficient charge transport capability. The sensor layer exhibits a generally lower degree of porosity as expected from the reduced laser impact at larger depths. Only a minor volume fraction of enclosed meso- and macropores was observed (e.g., unfilled pores in Figure 3C,D (left), Figure S5C, Supporting Information). A quite narrow transition zone between the sensor and transducer layer is corroborated by the cross-sectional analyses (Figure 3B,C). The foaming agent becomes pyrolyzed or partially transformed into graphitized carbon, whereas the porogen NaI (partially) evaporates, with NaI still being present in the sensor layer (Figure 3C, Na map).

In conjunction with the depth-dependent pore morphology, severe compositional and chemical bond gradients are revealed (Figure 3C,D). The gradient conversion of the precursors, both, from the sensor to the transducer layer as well as within the sensor layer from the core regions to the surfaces, is evident. The global preferential loss of nitrogen during carbonization[36] is depicted in Figure 3C,D (cf. N/C maps). The graphitized carbon skeleton of the central transducer layer did not show any nitrogen signals in EELS/EDXS. Occasionally, residual N-rich particles are found (Figure 3C,D, N map), which are explained by severe enthalpic cooling upon evaporation of the adjacent material.

Within the sensor layer, an abrupt depletion of the local nitrogen content in the shell regions is observed, while the composition of the core regions is rather constant (Figure 3D, N/C maps of sensor layer). Comparing that core composition after laser treatment, i.e., a concentration ratio of nitrogen:carbon ≈35:55 (at%), with the composition of the adenine-CNFA (Figure S1, Supporting Information) indicates a slight preferential loss of nitrogen. Substantial concentrations of oxygen of the order of 5 at% are present, both, in the transducer layer as well as the shell of the sensor layer due to the conversion in an oxygen environment (Figure 3D; Figure S5B, Supporting Information).

The strong thermal impact in the hot zone during laser treatment, which is the upper half of the device, yields the highly graphitized transducer layer as concluded from HRTEM, electron diffraction, 4D-STEM, EELS, and Raman microscopy (Figure 3F–H; Figures S5D and S7, Supporting Information).[37] Independent of the reaction atmosphere the surface Raman spectra show common features of a turbostratic graphitic material, i.e., the presence of pronounced D-, G-, and D'-bands, indicating a high degree of graphitization.[38] Notably, the LP_{O2}-$Ade380_{90}$/$Glu300_{10}$ sensor, processed in an oxygen atmosphere, shows a significantly higher degree of graphitization as only negligible contributions of sp[3]- and disorder-related D4 and D3 bands at 1200 and 1460 cm^{-1}, respectively, and a lower defect-attributed D-band are
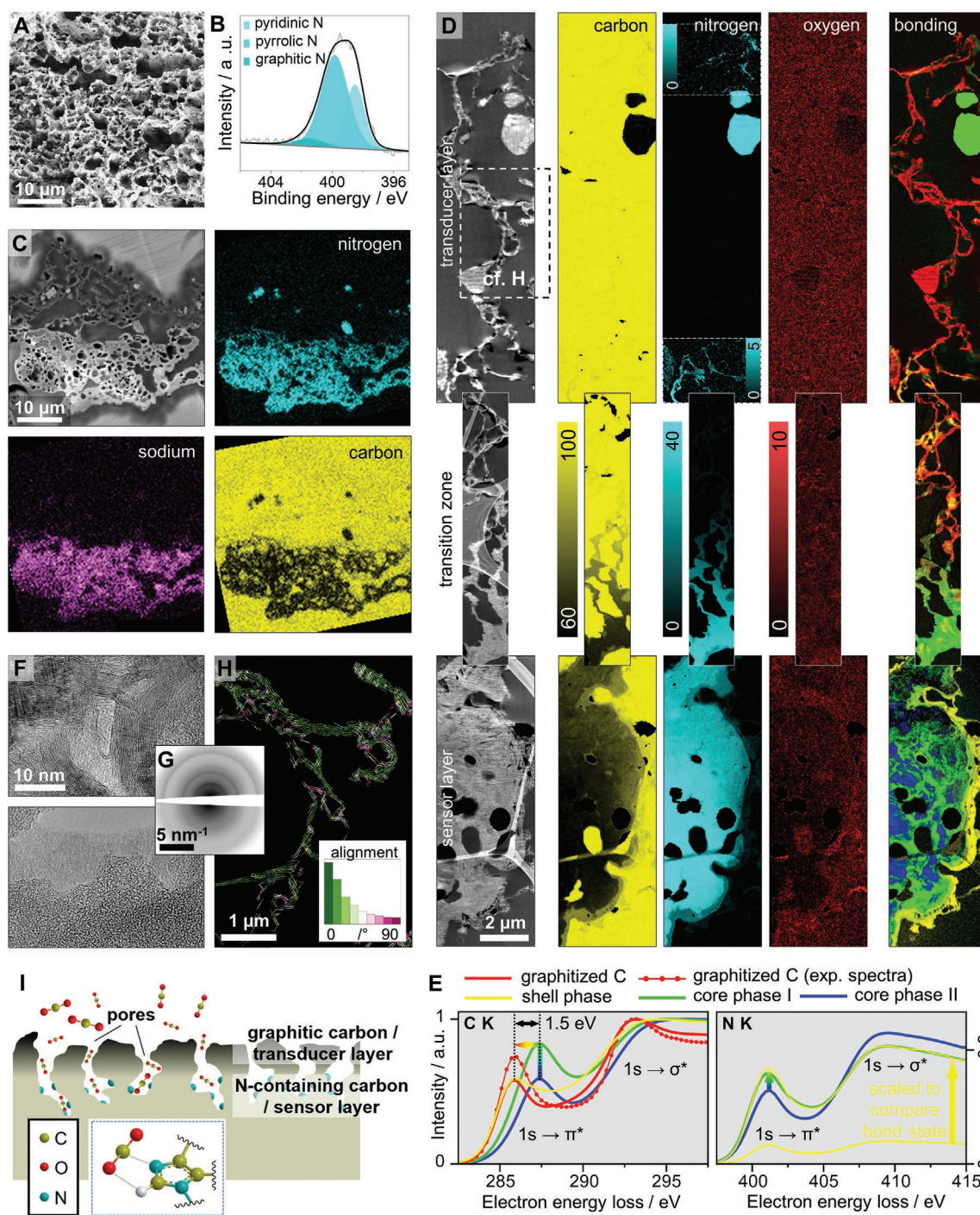
**ADVANCED
SCIENCE NEWS**

www.advancedsciencenews.com

**ADVANCED
FUNCTIONAL
MATERIALS**

www.afm-journal.de

Figure 3. Scale-bridging characterization of LP_{O2}-$Ade380_{90}$/$Glu300_{10}$ sensor: A) Top-view SEM micrograph; B) X-ray photoelectron spectrum with emphasis of the $N_{/1s}$ region; C) Cross-sectional backscatter SEM micrograph with correlated EDXS element maps (composition in at% with sum of C, N, O, Na being considered 100 at%); D) Cross-sectional TEM analyses (microtomic, epoxy-embedded cross-section) of representative regions (not necessarily adjacent) of the transducer and sensor layers as well as the transition zone: (left) HAADF-STEM micrographs with a few uninfiltrated pores (black), embedding epoxy resin (homogeneous dark gray), and superimposed lacey TEM support film (wavy horizontal contrast features in the STEM image of the sensor layer indicate slight thickness variations due to microtomic sectioning), (center) corresponding EELS element maps with color codes in at% (sum of C, N, O being considered 100 at%) with locally enhanced contrast in upper N map (0–5 at%) where nitrogen is present, (right) bond mapping showing distributions (weightings) of major phases identified by PCA (red: graphitized carbon, yellow: shell phase, green/blue: core phases I/II); E) Respective PCA spectra of those phases (details in Figure S6, Supporting Information) with selected energy-loss ranges of C and N ionization edges (background corrected, C edge normalized, N relative to C); F) Exemplary HRTEM images (overview images in Figure S5, Supporting Information) and G) SAED patterns of graphitized carbon and shell regions; H) Flowline visualization of local basal-plane orientation with respect to respective pore surface (ROI marked in D, details in Figure S5, Supporting Information): local misalignment angle between basal-plane normal and pore-surface normal according to color code in histogram (distribution of misalignment angles in inset); I) Schematic function of sensor.

observed.[39,40] In more detail, 4D-STEM revealed a strong interplay of local morphology and local crystal structure within the transducer layer. The systematic alignment of the surface-near graphite basal planes parallel to the local pore surfaces, indicated in individual HRTEM micrographs (e.g., Figure S5D, Supporting Information), is depicted on a global scale in Figure 3H and Figure S5E (Supporting Information) (cf. Figure 3D, explanation in Figure S5E, Supporting Information). The representative region of the transducer layer yielded more than 50% of the graphitic material (with (001) excited for evaluation) within only ± 20° misalignment (inset in Figure 3H).

The sensor layer is amorphous and shows several "phases" of different chemical compositions identified by principal component analysis of the EELS maps (blue/green/yellow in Figure 3D). Although the material is not in thermodynamic equilibrium, the term "phase" is used to describe regions of similar composition and structure. These phases show indications for evolving ordering with ongoing conversion (Figure 3F,G; Figure S6A in Supporting Information, the multiscattering resonance of C ionization edge of shell phase).

Two major aspects, which are CO_2-specific binding sites (nitrogen)[41–43] in conjunction with increased surface polarity by ionic groups (oxygen),[43] have been described in the literature that facilitates the adsorption of CO_2 in porous carbon materials. DFT calculations confirm a strong energetic interaction between CO_2 and N-containing functional groups, in particular to multi-N-containing species like imidazole units.[44] The laser treatment of LP_{O_2}-$Ade380_{90}$/$Glu300_{10}$ under high O_2 concentration enhances its surface polarity by introducing oxygen-containing groups such as C−O and C=O (Figure 3D; Figure S6, Supporting Information) and strongly enhances the response (Figure 2B). The specific binding of CO_2 is explained by the presence of pyrrolic N species (Figure 3B).[43]

For a correlation to the chemical bonding within the optimized sensor, surface X-ray photoelectron spectroscopy (XPS), global IR spectroscopy, and EELS bond analyses were performed. XPS confirms a high degree of carbonization and the presence of oxygen and nitrogen-containing functional groups by the prominent sp[2]-carbon peak at 284.6 and in the C_{1s} region and signals at 285.4, 286.1, and 287.5 eV assigned to sp[3]-carbon, C−N/C−O, and C=N/C=O, respectively (Figures S8–S10, Supporting Information). Oxygen is bound in the form of C=O, C−O (aliphatic), and C−O (aromatic) as evidenced by a set of three peaks at 531.3, 532.4, and 533.6 eV.[45] Most importantly, the N_{1s} area shows a prominent signal at 399.8 eV stemming from pyrrolic/imidazolic N and two minor peaks at 398.5 and 401.5 eV typical for pyridinic and graphitic N, respectively (Figure 3B).[46,47] Among the nitrogen functionalities, the pyrrolic/imidazolic species amount to 61%. This composition is independent of the addition of the foaming agent as it is also observed for the pure LP_{O_2}-Ade380 (Figure S8, Supporting Information). In accordance with the EELS bonding analysis, the XPS results support the interpretation of having imidazolic N groups as active sites but should not be interpreted as direct evidence.

Upon laser treatment of the pure adenine-CNFA as well as the optimized sensor, a variety of N functional groups is preserved in the N-containing phases of the lower layer. These functional groups are detected in the low-energy region of the FT-IR spectrum at 1064, 1241, and 1390 cm^{-1} (Figure S11,

Supporting Information). The latter two most likely originate from C−N stretching vibrations, either graphitic or pyrrolic/imidazolic N.[46,48] The XPS analysis shows a major content of pyrrolic/imidazolic N in the LP-NC films. It has been shown, that pyrrolic N decomposes at temperatures >600–800 °C.[49] The cross-sectional analyses of the sensor indicate that the laser-induced reaction temperatures in the sensor layer are lower, and thus a major part of the pyrrolic/imidazolic N is preserved after laser treatment.

Four major phases were identified throughout the device cross-sections by EELS bond analyses (Figure 3D(right),E; Figure S6, Supporting Information). Highly graphitized carbon (red, no N) constitutes the transducer layer[37] whereas the sensor layer consists of three N-containing phases, which are a shell phase (yellow) and two less transformed core phases I/II (green/blue) of the same composition but in different bond states.[36,50] The detailed discussion is given in the supporting information (Supporting Information, pp. S5–S8). In conclusion, very high degrees of sp[2] hybridization of both elements in all phases are confirmed with an increase in the early stage of the transformation from core phase II to I (Figure 3E, blue → green).[37] While the spectral data is governed by C=C bonds in the graphitized carbon and predominantly C=N bonds in both core phases with high N content, the dilution of N renders the shell phase a transition state (spectral superposition) between both extremes with both, C=C and C=N bonds present (Figure 3E).[36,51] Partial electron transfer from C to N causes the spectral shift by 1.5 eV.[51]

The sensor functionality is particularly attributed to those sp[2]-bound N species observed within the shell phase.[52,53] To distinguish between different pyrrolic/imidazolic/graphitic nitrogen functionalities on the nanometer or even atomic scale is, however, challenging due to the bulk characteristics of the spectra with manifold contributions from different atomic configurations.

As a reference, an LP-NC film from cytosine without pyrrolic nitrogen was prepared, which did not show any sensing response (Figure S12, Supporting Information). Although laser-treatment of cytosine produces LP-NC films with a high nitrogen content and similar resistivity and morphology,[31] the inherent absence of pyrrolic N in the precursor only generates non-active N-sites. As an additional reference experiment, we prepared laser-carbonized polyimide (well-known as laser-induced graphene (LIG)). Again, no sensing response toward CO_2 was observed (Figure S13, Supporting Information). Noteworthy, the influence of the charge carrier properties of the LP-NC on the sensor performance, tested by Hall measurements, is negligible (Figure S14, Supporting Information). Only the charge carrier mobility is slightly increased in the sensors produced under oxygen. We assume that the combustion supported by O_2 increases the effective reaction temperature, which leads to a higher degree of graphitization and thus a higher charge carrier mobility.

2.4. Sensor Performance

A comprehensive performance test of LP_{O_2}-$Ade380_{90}$/$Glu300_{10}$ (thickness 100 μm), was conducted (**Figure 4**). The maximum
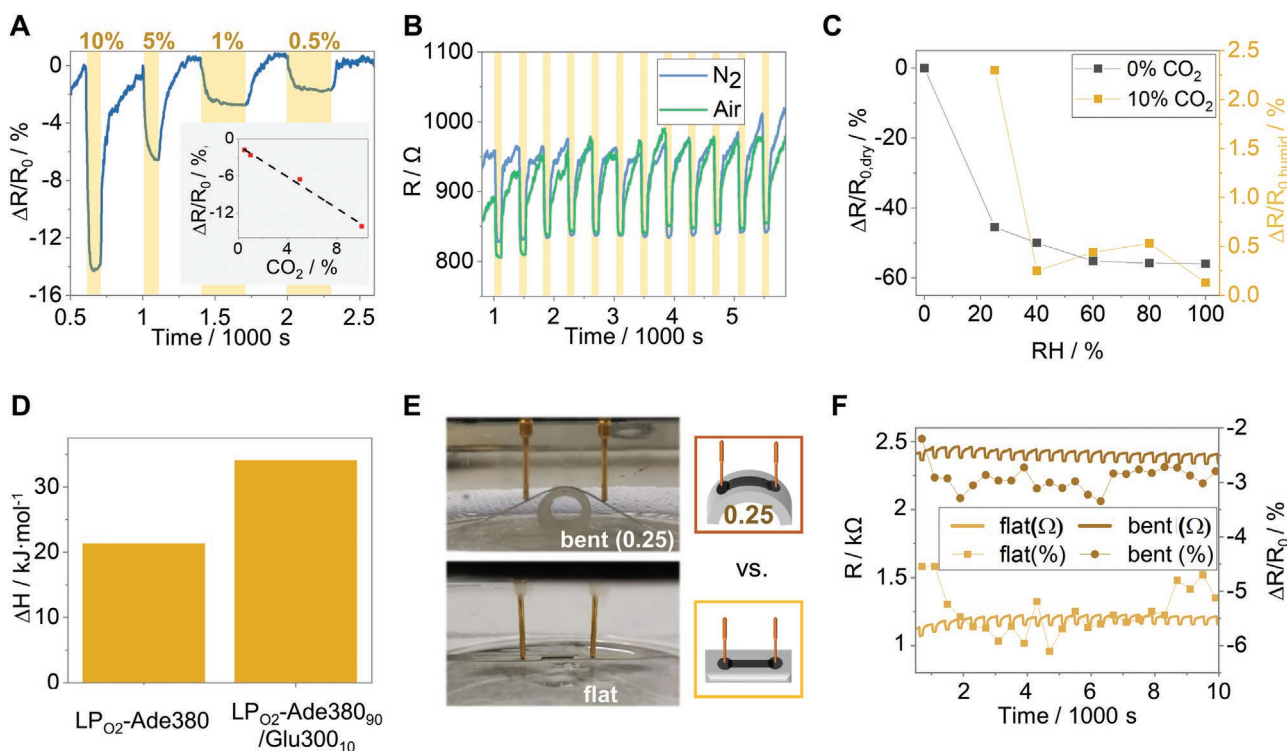
Figure 4. Performance of LP_{O_2}-$Ade380_{90}$/$Glu300_{10}$ sensor: A) Resistance response toward exposure to different CO_2 concentrations in N_2 as carrier gas; B) Resistance response toward 10% of CO_2 using N_2 (blue) or dry air (green) as carrier gas; C) Resistance response toward different relative humidities in the N_2 carrier gas (black) and to 10% CO_2 (90% N_2) at different humidities (orange); D) Values of $\Delta_{ads}H$ for CO_2 on the LP_{O_2}-$Ade380_{90}$/$Glu300_{10}$ sensor in comparison to the reference LP_{O_2}-$Ade380$; E) and F) Resistance response of a sensor with a thickness of 75 μm toward 10% of CO_2 upon bending (curvature: 0.25 mm^{-1}) (brown) compared to the flat state (orange) (N_2 carrier gas).

response values $\Delta R/R_0$ of that sensor to different concentrations of CO_2 follow a linear trend (Figure 4A) indicating that no saturation is reached at the maximum tested analyte concentrations. Even at 0.5% CO_2 a reasonable response of $\Delta R/R_0 = -1.8\%$ is achieved. Fitting of the data in Figure 4 yields a sensitivity of S = -1.28×10^{-6} ppm^{-1}. The response is stable upon cycling and is identical in air and N_2 as carrier gases (Figure 4B). The response and recovery times during cycling are the same in both environments with $t_{res} = 25$ s and $t_{rec} = 60$ s. Consequently, the presence of O_2 does not influence the detection mechanism. In addition, the optimized film LP_{O_2}-$Ade380_{90}$/$Glu300_{10}$ shows a rather low sensing response to the volatile organic compounds (VOCs) acetone and ethanol as interference analytes (Figure S15, Supporting Information).

The sensing performance was further characterized at different relative humidities (RH) (Figure 4C). Naturally, polar LP-NC surfaces show a high affinity to adsorption of H_2O which is usually orders of magnitude higher than CO_2 due to its electron-accepting character.[43] Although LP_{O_2}-$Ade380_{90}$/$Glu300_{10}$ shows a very strong and fast response to H_2O (up to $\Delta R/R_0 = 50\%$ in RH = 100%, Figure S16, Supporting Information), stable selective response to CO_2 even at such high relative humidity levels is detectable (Figure S17, Supporting Information). For example, in the range of RH of 40–80%, the response increases from $\Delta R/R_0 = 0.25$ to 0.53% (Figure 4C). This supports the hypothesis of selective binding sites for CO_2. In

comparison, also nanocarbon-based gas sensors show a strong relative response to H_2O. Typical strategies for achieving selectivity are compositing with selective moieties such as polypyrrole or nitrogen doping.[7–9]

To understand the interaction between the LP-NCs and water/CO_2 the standard enthalpy of adsorption $\Delta_{ads}H^0$ was determined using a simple Langmuir's model: a monolayer of adsorbed analyte (CO_2 or H_2O) without interaction between each other is present at the sensor surface in equilibrium with gaseous analyte molecules. Assuming that the change of the sensor resistance is proportional to the quantity of adsorbed analyte, the transitory regime of the sensing curves is fitted to determine the adsorption equilibrium constants at different temperatures (Figures S18-S21 and Tables S2-S3, Supporting Information). Finally, the standard enthalpy of analyte adsorption $\Delta_{ads}H$ on the sensor surface is determined according to the Van't Hoff equation. The optimized sensor shows very large $\Delta_{ads}H^0$ values of 34.1 kJ·mol^{-1} for CO_2 in comparison to only 21.3 kJ·mol^{-1} for the reference LP_{O_2}-$Ade380$ (Figure 4D). Similar values for $\Delta_{ads}H°$ for CO_2 adsorption in porous N-containing carbons are reported for CO_2.[43] The increase upon glucose addition is attributed to the foaming effect in LP_{O_2}-$Ade380_{90}$/$Glu300_{10}$, resulting in a higher amount of exposed pyrrolic/imidazolic N and a larger interaction with the CO_2 molecules for a given quantity of sensor material. Notably, the method is not suitable for the determination of $\Delta_{ads}H^0$ values for water (Figures S18-S21, Supporting Information).

ADVANCED
SCIENCE NEWS

www.advancedsciencenews.com

ADVANCED
FUNCTIONAL
MATERIALS

www.afm-journal.de

The sensing properties are retained upon mechanical deformation for a sensor strip with a thickness of 75 μm. The change in resistance ΔR upon defined bending was quantified using a movable electrode stage connected to a four-probe multimeter (Figure S22, Supporting Information). It is reversible and comparable to previously analyzed LP-Cs.[32] In order to simulate the bending of the sensor film on the finger (Figure S23, Supporting Information), we placed a flexible hose with a diameter of ≈6 mm under the sensor film resulting in a curvature of 0.25 mm⁻¹ determined by translating the shapes from photographs into x-y data using the freeware Engauge Digitizer. Then the sensor performance in the bent state was analyzed in the gas-sensing cell (Figure 4E,F) (1000 s, 24 cycles). Details of the experiment are given in the Supporting Information (pp S16). For comparison, the same sensor strip was analyzed in a flat state. Independent of the curvature, a stable response is observed. Figure 4F demonstrates that the absolute change in resistance ΔR, the feedback upon CO_2 loading, is retained upon bending, whereas the resistance baseline shifts toward higher values with increasing deformation. Consequently, the relative response in the bent state is just about half of that in a flat configuration ($\Delta R/R = -2.9$ vs -5.7%). The observed baseline change by a factor of around two for the curvature of 0.25 mm⁻¹ is in agreement with previous results about mechanical LP-(N)C sensors.[32] Moreover, the response and recovery times, t_{res} and t_{rec}, are the same. From the proposed functions of the transducer and sensor layers, such behavior has to be expected because both, the efficiency/density of the chemical binding sites for CO_2 as well as their accessibility through the still highly porous transducer layer, are hardly altered by such a degree of deformation.

To demonstrate its applicability, the LP$_{O2}$-Ade380$_{90}$/Glu300$_{10}$ sensor was used to repeatedly measure the CO_2 level in exhaled breath (Figure S23, Supporting Information). Therefore, the flexible sensor was directly placed under ambient conditions without the need for a mask. In view of their rapid response, high sensitivity, and good selectivity under ambient conditions as well as their mechanical properties, the developed LP-NC sensors may prospectively be employed as real-time wearable breath detection sensors.

3. Conclusions

The depth-dependent laser-induced conversion of organic precursor coatings has successfully been utilized to fabricate a complete flexible sensor architecture for selective CO_2 sensing at room temperature. The method exhibits decisive advantages for producing N-containing carbons from adenine as a precursor: the gradual carbonization induces the formation of a graphitized transducer layer but retains the active binding sites in the less impacted, buried sensor layer. By introducing glucose as an efficient foaming agent, the sensitivity is enhanced, as it systematically opens pore channels to access those active species. In turn, the active sites, i.e., imidazolic nitrogen, are preserved in the lower sensor layer. Systematic optimization of the sensor morphology and surface chemistry resulted in a drastic performance increase of almost two orders of magnitude.

The introduced fabrication route, based on mostly abundant organic precursors, is highly versatile as it facilitates the utilization of chemical functionalities of the primary ink by a simple one-step laser writing process. The well-defined morphology and chemical functionality of those sensor architectures may be tailored for other applications by changing/optimizing the vast process parameters including the selected precursor materials with their specific functionalities, the ink composition, the primary coating thickness, the substrate, the laser-treatment parameters, and the conversion environment. The proposed concept provides a materials synthesis strategy for chemical sensors integratable into sensor array technologies which may lead to application in wearable, easy-to-operate, and real-time sensing devices. The conceptual development for the simultaneous read-out during flexible operation is the subject of future feasibility studies.

4. Experimental Section

Chemicals and Materials: Adenine (>99%, TCI Europe N.V.), D-glucose (anhydrous, Fisher Scientific GmbH), ethylene glycol (>99.7%, AnalaR Normapur, VWR Chemicals), polyvinyl-pyrrolidone (average mol wt. 10000, Sigma Aldrich), sodium iodide (99.5%, Alfa Aesar) were used as received. The PET substrates with a thickness of 170 μm were Melinex sheets obtained from Plano GmbH.

Preparation of the CNFAs: Glu300 and Ade300-400 were prepared by loading 1 g of D-glucose or 2 g of adenine into an alumina crucible or a quartz glass boat with a lid and heating at different temperatures between 300 °C and 400 °C in a tube furnace with a heating rate of 3 K min⁻¹. A gentle stream of N_2 (0.1 L min⁻¹) was ensured during the reaction. The hold-time was 2 h. The reaction products were retained and grinded in a ball mill (diameter of the ball: 1 cm) for 1 h with a speed of 600 rpm to obtain finely powdered products Glu300 or Ade300-380 (Figure S1, Supporting Information).

Preparation of the Primary Coatings: Polyvinylpyrrolidone (PVP) (Film-forming agent) was dissolved in EtGly to obtain a 0.2 g mL⁻¹ solution (PVP/EtGly).[35] Sodium iodide (0.4 g mL⁻¹) was added and dissolved.[34] The solution was added to the CNFA and gently stirred for 24 h to obtain homogeneous inks. The samples are labeled according to: CNFA1$_{content}$(/CNFA2$_{content}$), e.g., Ade380 and Glu300 as CNFAs synthesized from adenine and glucose by pre-carbonization at 380 °C and 300 °C, respectively. All concentrations of the different samples with respect to the volume of the solvent are given in **Table 1**. A drop of the ink was applied onto the substrate and the ink was doctor bladed with a blade distance between 300 and 500 μm. Ethylene glycol was then evaporated at 80 °C on a precision hotplate (PZ2860-SR, Gestigkeit GmbH) to obtain the final films with thicknesses between 30–100 μm. The thickness was determined with a digital micrometer or vertical scanning interferometry.

Laser-Carbonization: Laser-carbonization was conducted with a high-precision laser engraver setup (Speedy 100, Trotec) equipped with a 60 W CO_2 laser. Focusing was achieved with a 2.5-inch focus lens providing a focal depth of ≈3 mm and a focus diameter of $d = 170$ μm. The center wavelength of the laser is 10.6 ± 0.03 μm. The scanning speed v, generically given in %,

Table 1. The concentrations of components in the inks.

Inks	Ade300-400 [g mL^{-1}]	Glu300 [g mL^{-1}]	EtGly/PVP [µL]
Ink_Ade300-Ade400	0.57	0	350
Ink_Glu300	0	0.47	430
	Ade380 [g mL^{-1}]	Glu300 [g mL^{-1}]	EtGly/PVP [µL]
Ink_Ade380$_{10}$/Glu300$_{90}$	0.06	0.51	350
Ink_Ade380$_{20}$/Glu300$_{80}$	0.11	0.46	350
Ink_Ade380$_{35}$/Glu300$_{65}$	0.2	0.37	350
Ink_Ade380$_{50}$/Glu300$_{50}$	0.29	0.29	350
Ink_Ade380$_{65}$/Glu300$_{35}$	0.37	0.2	350
Ink_Ade380$_{80}$/Glu300$_{20}$	0.51	0.06	350
Ink_Ade380$_{90}$/Glu300$_{10}$	0.51	0.06	350

was converted into cm·s^{-1}. The effective output power P in watts of the laser was measured with a Solo 2 (Gentec Electro-Optics) power meter. The resulting energy input per area (or fluence) F in J·cm^{-2} in the vector mode onto the film is given by

$$F = \frac{P}{v \cdot d} \tag{1}$$

For the experiments, the laser settings were adjusted to meet the requirements of the films according to **Table 2**. A standard sensor strip is made of five parallel lines of 5 mm in length distributed across a width of 0.5 mm. An open-top atmospheric chamber was designed to generate a continuous flow of a selected gas (O$_2$ or N$_2$) for the fabrication of LP-NC under controlled gas atmospheres (Figure S3, Supporting Information). The laser-patterned (LP) samples are labeled according to: LP$_{atmosphere}$–CNFA1$_{content}$(/CNFA2$_{content}$), e.g., LP$_{O2}$–Ade380$_{90}$/Glu300$_{10}$ for a laser-patterned film of a mixture of Ade380:Glu300 (90:10 wt.%) as CNFAs under O$_2$ reaction atmosphere.

CO$_2$ Sensing: The sensor platforms were placed in a gas-proof glass flow cell ($V_{cell} \approx 0.1$ L) and their ends were connected to two electrode bins. The electrical characterization was performed with an impedance unit at a frequency of 80 Hz and an alternating current (AC) of 0.05 mA for all measurements.

The total flow of gas mixtures was set to 1 L min^{-1}. Concentrations of 0.5%, 1%, 5%, and 10% CO$_2$ with respect to the total flow were controlled by mass flow controllers (GF040, Brooks Instrument GmbH). Humidity was controlled by a humidity generator (HUMIgen-04, Dr. Wernecke Feuchtemesstechnik). The sensitivity of the sensor was calculated according to

$$S = \frac{\Delta R}{R_0 \cdot \Delta C} \tag{2}$$

Langmuir's model was used to describe the interaction between the gas molecules and the sensor surface. At a given temperature, the fraction of occupied sites on the sensor surface is θ. The equilibrium constant of adsorption K is defined as the ratio between the rate constants of adsorption k_A and desorption k_D. The variation of θ is given by Equation 3, where P_A is the partial pressure of the analyte in the gas phase:

$$\theta = \frac{K * P_A}{1 + K * P_A} \tag{3}$$

When molecules are adsorbed on the surface of the LP-NC, the resistivity decreases. Then θ is given by:

$$\theta = \alpha * \left(R_0 - R_{eq} \right) \tag{4}$$

where R_0 is the initial resistance, R_{eq} is the resistance at equilibrium, α is the proportionality coefficient.

The heat of adsorption of CO$_2$ or H$_2$O was determined according to the van 't Hoff equation.

$$\frac{d(lnK)}{dT} = \frac{\Delta H_{ads}}{RT^2} \tag{5}$$

Bending Experiments: The experiments were performed with a homemade movable stage. The PET-supported sample strip was mounted between two electrodes (one movable) at a distance of 25 mm and bent in a positive (upwards) direction (Figure S20, Supporting Information). To provide a better electrical contact both ends of the carbon strip were connected with silver paint. The curvature of the bending was determined by translating the shapes from photographs into x-y data using the freeware Engauge Digitizer. The curvature is defined as the inverse radius at the maximum point of bending.

Sample Preparation for Electron Microscopy: Cross-sectional preparation of the sensors was conducted by ultramicrotomy utilizing a Leica EM UC7 microtome. Individual sensor strips were separated by doctor-blade cutting and embedded in epoxy resin (Araldite 502, Science Services, Germany) to facilitate the sectioning of the highly porous sensor heterostructures. Impregnation of the pores was supported by evacuation and subsequent pressurization of the uncured resin using a dedicated pressure vessel (miniclave steel, Büchi AG, Switzerland). Curing was carried out overnight at 60 °C. To create a trapezoid-shaped block face and to remove potentially damaged sample regions from cutting, trimming with a diamond knife (DiATOME 45° trim knife) was performed. A DiATOME 45° ultrasonic diamond knife was employed to obtain cross-sectional

Table 2. Laser parameters used in the experiments to fit the coating thickness.

Samples	Thickness [µm]	Power % [generic]	Power W	Speed % [generic]	Speed cm s^{-1}]	Fluence [J cm^{-2}]
LP_Glu300	75	2.20	1.12	0.30	0.53	125
LP_Ade380	75	2.10	1.07	0.30	0.53	119
LP$_{O2/N2/air}$_Ade380$_{90}$/Glu300$_{10}$	45	1.90	0.97	0.30	0.53	108
	75	2.10	1.07	0.30	0.53	119
	100	2.20	1.12	0.30	0.53	125

**ADVANCED
SCIENCE NEWS**

www.advancedsciencenews.com

**ADVANCED
FUNCTIONAL
MATERIALS**

www.afm-journal.de

TEM samples with minimal compression. The floating sections (deionized water) were transferred onto lacey carbon TEM grids (Plano AG) to provide sufficient support at reduced impact during EELS measurements. The resulting block face was used for complementary analysis by optical microscopy (OM) and environmental SEM.

5. Instrumental

5.1. Scanning Electron Microscopy

Top-view scanning electron microscopy with secondary electrons was performed on a Zeiss LEO 1550-Gemini field-emission microscopes (acceleration voltage: 3–10 kV). Cross-sectional EDXS element mapping and related imaging with back-scattered electrons of the embedded sensors (microtomy block surface) were performed using an environmental FEI Quanta 250 FEG-SEM. The instrument is equipped with an Apollo XL SSD detector for energy-dispersive X-ray spectroscopy and a differential pumping system to allow operation at low-vacuum levels for minimal charging. EDXS element maps were obtained at 5 keV primary electron energy to obtain sufficient count rates at the best achievable lateral resolution under low-vacuum conditions ($\approx$100 Pa).

5.2. Transmission Electron Microscopy

For bright-field transmission electron microscopy (bright-field TEM, BFTEM), selected-area electron diffraction (SAED, selected area diameter 150 nm), and high-resolution TEM (HRTEM), a FEI TitanX 60–300 TEM (NCEM/LBNL) (Schottky emitter, super twin objective lens, no aberration corrector, operated at 200 kV acceleration voltage) with Gatan 2k Ultrascan CCD camera was utilized. A gold particle sample was used to calibrate microscope magnification and camera length.

High-angle annular dark-field Scanning TEM (HAADF-STEM) in conjunction with electron energy-loss spectroscopy (EELS) were carried out using an FEI Talos F200X S/TEM (MNaF/Univ. Siegen) at 200 kV acceleration voltage. The microscope is equipped with an XFEG high-brightness gun and a Gatan Continuum ER spectrometer (with high-speed DualEELS, DigiScan, EDXS integration, GMS 3.5x). The acceleration voltage of 200 kV was chosen as a compromise between the mean-free path for inelastic scattering (EELS) and electron-beam induced damaging, the latter being minimized by sub-pixel scanning during EELS mapping acquisition.

EELS mappings were acquired from representative areas of the microtomic sensor cross-sections, which exhibit excellent and homogeneous relative thicknesses of t/$\lambda \approx 0.35 - 0.5$ depending on the local sensor density ($\approx$0.25 for the adjacent embedding epoxy due to the lower density). Dual EELS mappings (step size $\approx$20 nm) with core loss spectra in the energy-loss range of 200–800 eV (dispersion 0.3 eV/channel, ratio convergence/acceptance angle $\approx$2) were recorded to cover the essential ionization of C, N, and O at $\approx$285, 400, and 532 eV, respectively. Energy calibration was employed utilizing the respective low-loss datasets.

EELS element distributions for C, N, and O were derived by quantification with theoretical cross-sections as implemented in the Gatan software. For background correction, a power law function for C, O but a 1st-order log-polynomial function for N were employed (pre-edge fit range for all elements: 50 eV, post-edge fit ranges: 50 eV (C) and 25 eV (N, O)). As hydrogen as well as Na, I are not accessible in the recorded spectra range, the presented atomic concentrations refer to $c_C + c_N + c_O = 100$ at%.

To unravel variations of the local bond states within the sensor cross-sections without a priori knowledge of the resultant reaction products, principal component analysis (PCA), as implemented in GMS 3.40 (with Varimax orthogonal matrix rotation)[54] was applied to the recorded EELS datasets. As a result, PCA components were obtained, which describe individual phases, meaning, which include all three ionization edges, rather than individual element-specific signals. The spatial distributions in the main manuscript depict the lateral weighting factors of those identified components/phases. Due to better statistics, however, the phase-specific PCA components were separated into their C, N, and O contributions (independent background correction for each ionization edge), normalized with respect to the maximal intensity of the C K ionization edge, and presented throughout the manuscript. To verify the validity of those obtained spectral PCA distributions, 50 experimental spectra were selected from the respective mapping datasets, summed, normalized, and compared to the corresponding spectral PCA components (Figure S6, Supporting Information). The major challenges and limitations of PCA in this study are in detail discussed in the supporting material (pp. S5–S7, Supporting Information).

Experimental 4D-STEM datasets were acquired using the TEAM I instrument (NCEM/LBNL), a double aberration-corrected Thermo Fisher Titan fitted with a Gatan Continuum energy filter and K3 direct electron detector (operated in electron counting mode, 4x binning).[55] The energy-filtered diffraction patterns (15 eV slit width, central beam covered by 2.5 mrad beam stop) were acquired at an accelerating voltage of 300 kV in microprobe mode with a beam convergence semi-angle of 0.7 mrad (beam diameter $\approx$2 nm, beam current 70 pA) and a covered spectrometer semi-angle of maximum 21 mrad. A shadow image of the sample (i.e., a strongly defocused image of the STEM probe) was recorded to align the rotation between the scan field and recorded diffraction patterns. The datasets were evaluated employing the py4DSTEM software package.[56] Details are provided in the supporting information. Fourier-transform infrared spectroscopy

FT-IR spectroscopy was performed using a Nicolet iS 5 FT-IR-spectrometer in conjunction with an iD7 ATR unit from ThermoFisher Scientific. The LP-NC powder was scratched off the PET substrate and directly analyzed.

5.3. Raman Spectroscopy

Raman spectra were obtained with a confocal Raman Microscope (alpha300, WITec, Germany) equipped with a piezo-scanner (P-500, Physik Instrumente, Karlsruhe, Germany). The laser, λ = 532 nm was focused on the samples through a 50× objective. The laser power on the sample was set to 5.0 mW.

**ADVANCED
SCIENCE NEWS**
www.advancedsciencenews.com

**ADVANCED
FUNCTIONAL
MATERIALS**
www.afm-journal.de

5.4. Hall Measurements

The electrical conductivity σ of carbonized films was determined at room temperature by the van der Pauw method[57] in a Hall effect measurement system 8404 (Lake Shore Cryotronics, Inc.). The samples, all shaped in precise cloverleaf geometry with a 10 mm diameter, were placed on a commercial 10 mm prober pin sample card of the 8404 Hall effect measurement system. Excitation currents from −5 to +5 mA have been used for the $I–V$ measurements. All the $I–V$ curves for all four different four-probe contact configurations show the expected linear behavior.

Both, the DC and the Double AC Hall method[58,59] employing two MFLI lock-in amplifiers (Zurich Instruments AG) and a CS580 voltage-driven current source (Stanford Research Systems) have been applied in the same setup to determine the charge carrier concentration. Different sets of oscillating excitation current ($I = 2$ to 6 mA with frequency $f_I = 88$ Hz) and magnetic field (0.08, 0.16, and 0.23 T with frequency $f_B = 0.8$ Hz) have been used to measure the Hall voltage $V_H = V(f_I + f_B) + V(f_I − f_B)$, automated by a home made LabVIEW program. The linear relationship between V_H and $I \times B$ (Equation 6) is used to calculate the charge carrier density

$$p = \frac{1}{et} \frac{\partial(I \times B)}{\partial V_H} \tag{6}$$

where e is the elementary charge and t is the thickness of the sample. The charge carrier mobility μ was calculated by the formula $\mu = \frac{\sigma}{pe}$.

5.5. X-Ray Photoelectron Spectroscopy

XPS measurements were performed at the ISISS beamline of the synchrotron radiation facility BESSY II of Helmholtz-Zentrum Berlin, Germany. The used endstation consisted of a bending magnet (D41) and a plane grating monochromator (PGM) in the soft X-ray range 80–2000 eV with an 80–200 µm beam spot. The photoelectron analyzer is provided by SPECS GmbH (Phoibos 150) hemispherical analyzer. In order to minimize losses of photons and electrons, a 50 nm thick SiNx X-ray membrane close to the sample was used. Each sample was fixed on the sapphire sample holder. XPS spectra were analyzed through CasaXPS and Igor Pro. The spectra were deconvoluted with a combined Gaussian and Lorentzian function after a Shirley + linear background subtraction.

Supporting Information

Supporting Information is available from the Wiley Online Library or from the author.

Acknowledgements

Conflict of Interest

The authors declare no conflict of interest.

Author Contributions

H.W.: Investigation, Conceptualization, Methodology, Validation, Writing – Original Draft; C.O.O.: Investigation, Methodology, Validation, Writing – Original Draft; G.P.: Investigation, Methodology, Validation, M.H.: Investigation, Methodology, Validation; S.D.: Investigation, Methodology, Validation; D.C.: Investigation, Methodology, Validation; D.K.: Investigation, Methodology, J.C.: Investigation, Methodology, Validation; C.O.: Investigation, Methodology, Validation; A.K.-G.: Supervision; K.H.: Writing – Review & Editing, Supervision; B.B.: Conceptualization, Supervision, Methodology, Validation, Writing – Original Draft, Writing – Review & Editing; V.S.: Conceptualization, Methodology, Validation, Writing – Original Draft, Writing – Review & Editing, Supervision, Project administration.

Data Availability Statement

The data that support the findings of this study are available from the corresponding author upon reasonable request.

Keywords

[1] N. Oreskes, *Science* **2004**, *306*, 1686.
[2] W. Ripple, *Bioscience* **2019**, *70*, 8.
[3] K. Permentier, S. Vercammen, S. Soetaert, C. Schellemans, *Int. J. Emerg. Med.* **2017**, *10*, 17.
[4] R. D. Manzanedo, P. Manning, *Sci. Total Environ.* **2020**, *742*, 140563.
[5] S Mulmi, V. Thangadurai, *J. Electrochem. Soc.* **2020**, *167*, 037567.
[6] T. M. Swager, K. A. Mirica, *Chem. Rev.* **2019**, *119*, 1.
[7] Y. Lin, Z. Fan, *Mater. Sci. Semicond. Process.* **2020**, *107*, 104820.
[8] E. Llobet, *Sensors Actuators, B Chem* **2013**, *179*, 32.
[9] K. R. Ratinac, W. Yang, S. P. Ringer, F. Braet, *Environ. Sci. Technol.* **2010**, *44*, 1167.
[10] C. Wang, *Adv. Mater.* **2019**, *31*, 1903491.

[11] D. Yu, *Energy & Fuels* **2018**, *32*, 3726.

[12] J. W. F. To, *J. Am. Chem. Soc.* **2015**, *138*, 1001.

[13] J. Wei, *Adv. Func. Mater.* **2013**, *23*, 2322.

[14] J. Gong, M. Antonietti, J. Yuan, *Angew. Chemie* **2017**, *129*, 7665.

[15] W. Ju, *Nat. Commun.* **2017**, *8*, 944.

[16] M. Sevilla, P. Valle-Vigón, A. B. Fuertes, *Adv. Funct. Mater.* **2011**, *21*, 2781.

[17] V. Chandra, *Chem. Commun.* **2012**, *48*, 735.

[18] S. R. Venna, M. A. Carreon, *J. Am. Chem. Soc.* **2010**, *132*, 76.

[19] Y. Yang, *Nat. Biotechnol.* **2020**, *38*, 217.

[20] M. G. Stanford, K. Yang, Y. Chyan, C. Kittrell, J. M. Tour, *ACS Nano* **2019**, *13*, 3474.

[21] A. R. Cardoso, *Biosens. Bioelectron.* **2019**, *124–125*, 167.

[22] G. Xu, Z. A. Jarjes, V. Desprez, P. A. Kilmartin, J. Travas-Sejdic, *Biosens. Bioelectron.* **2018**, *107*, 184.

[23] C. Fenzl, *ACS Sens.* **2017**, *2*, 616.

[24] W. Yang, *ACS Appl. Mater. Interfaces* **2020**, *12*, 3928.

[25] L. Q. Tao, *Nat. Commun.* **2017**, *8*, 14579.

[26] Y. Wang, Y. Wang, P. Zhang, F. Liu, S. Luo, *Small* **2018**, *14*, 1802350.

[27] L. Huang, J. Su, Y. Song, R. Ye, *Nano-Micro Lett.* **2020**, *12*, 157.

[28] M. F. El-Kady, V. Strong, S. Dubin, B. K. R. , *Science* **2012**, *335*, 1326.

[29] J. Lin, *Nat. Commun* **2014**, *5*, 5.

[30] R. Ye, *Adv. Mater.* **2017**, *29*, 1702211.

[31] H. Wang, *Carbon N. Y.* **2021**, *176*, 500.

[32] M. Hepp, et al., *npj Flex. Electron.* **2022**, *6*, 3.

[33] X. X. Wang, et al., *Nat. Commun.* **2013**, *4*, 2905.

[34] H. Wang, *Adv. Funct. Mater.* **2021**, *31*, 2104061.

[35] S. Delacroix, H. Wang, T. Heil, V. Strauss, *Adv. Electron. Mater.* **2020**, *6*, 2000463.

[36] F. Ramos, TEM, in *Electron Microscopy and Analysis*, U.K. Institute of Physics Publishing, Bristol **1999**. 381–384.

[37] H. Daniels, R. Brydson, B. Rand, A. Brown, *Philos. Mag.* **2007**, *87*, 4073.

[38] D. B. Schuepfer, *Carbon N. Y.* **2020**, *161*, 359.

[39] A. Sadezky, H. Muckenhuber, H. Grothe, R. Niessner, U. Pöschl, *Carbon N. Y* **2005**, *43*, 1731.

[40] M. Pawlyta, J. - N. Rouzaud, S. Duber, *Carbon N. Y.* **2015**, *84*, 479.

[41] Y. Zhao, X. Liu, Y. Han, *RSC Adv.* **2015**, *5*, 30310.

[42] Y. Zhao, X. Liu, K. X. Yao, L. Zhao, Y. Han, *Chem. Mater.* **2012**, *24*, 4725.

[43] M. Oschatz, M. Antonietti, *Energy Environ. Sci.* **2018**, *11*, 57.

[44] H. M. Lee, I. S. Youn, M. Saleh, J. W. Lee, K. S. Kim, *Phys. Chem. Chem. Phys.* **2015**, *17*, 10925.

[45] M. Smith, L. Scudiero, J. Espinal, J. S. McEwen, M. Garcia-Perez, *Carbon N. Y.* **2016**, *110*, 155.

[46] P. Lazar, R. Mach, M. Otyepka, *J. Phys. Chem. C* **2019**, *123*, 10695.

[47] R. C. Dante, *Carbon N. Y.* **2017**, *121*, 368.

[48] A. Misra, P. K. Tyagi, M. K. Singh, D. S. Misra, *Diam. Relat. Mater.* **2006**, *15*, 385.

[49] J. R. Pels, F. Kapteijn, J. A. Moulijn, Q. Zhu, K. M. Thomas, *Carbon N. Y.* **1995**, *33*, 1641.

[50] A. Jaleel, et al., *Chem. Eng. J.* **2022**, *433*, 133571.

[51] A. Fernández, et al., *Appl. Phys. Lett.* **1996**, *69*, 764.

[52] M. Demir, et al., *Int. J. Energy Res.* **2018**, *42*, 2686.

[53] F. Alvarez, M. C. dos Santos, *J. Non. Cryst. Solids* **2000**, *266–269*, 808.

[54] G. Lucas, P. Burdet, M. Cantoni, C. Hébert, *Micron* **2013**, *52–53*, 49.

[55] C. Ophus, *Microsc. Microanal.* **2019**, *25*, 563.

[56] B. H. Savitzky, *Microsc. Microanal.* **2021**, *27*, 712.

[57] L. J. v. d. Pauw, *Philips Res. Reports* **1958**, *13*, 1.

[58] P. Chu, S. Niki, J. W. Roach, H. H. Wieder, *Rev. Sci Instrum.* **1987**, *58*, 1764.

[59] A. Kasai, A. Abdulla, T. Watanabe, M. Takenaga, *Jpn. J. Appl. Phys.* **1994**, *33*, 4137.